Research Square

Preprints are preliminary reports that have not undergone peer review.
They should not be considered conclusive, used to inform clinical practice,
or referenced by the media as validated information.

Near-Neutral Aqueous Proton Batteries: Electrolyte Design and Proton Transport Mechanisms

Xiang Cai

caixiang@dlpu.edu.cn

Dalian Polytechnic University https://orcid.org/0009-0009-2006-1234

Qiyao Shao

Dalian Polytechnic University

Huan Liu

Dalian Institute of Chemical Physics, Chinese Academy of Sciences

Jiaqi Li

Dalian Polytechnic University

Kuixuan Zhang

Dalian Polytechnic University

Article

Keywords: proton batteries, amino acid salt electrolytes, L-lysine phosphate, structural diffusion, vehicular diffusion

Posted Date: May 4th, 2026

DOI: https://doi.org/10.21203/rs.3.rs-9298626/v1

License: This work is licensed under a Creative Commons Attribution 4.0 International License.
Read Full License

Additional Declarations: There is **NO** Competing Interest.

Abstract

Proton batteries operate via a typical rocking chair mechanism, which endows them with great potential to yield a high energy density owing to their electrolytes without participation in full cell reaction. Employing aqueous inorganic acid electrolytes or the equivalents where protons are transported effortlessly both in their bulk phase and at their electrochemical interface via the structural diffusion is one of the basic requirements to trigger the rocking chair mechanism. However, a high free proton concentration resulting from it inevitably restricts an increase in the operating voltage and impedes the application of some active materials with inferior resistance to acid corrosion. Herein, a novel liquid-state H^+ conductor prepared by reacting L-lysine with phosphoric acid in an aqueous medium is demonstrated as an electrolyte for proton batteries and renders them operational not only via the rocking chair mechanism but also in a near-neutral electrolyte environment. L-lysine molecules capture the free protons via the protonation at the ε and α amino groups, leading to the formation of the near-neutral electrolyte environment. The generated L-lysine ions are typical of the electromigration of cations and transport the protons in the bulk phase of the electrolyte via the vehicular diffusion. By contrast, the carboxy group of the L-lysine ions enables the facile proton transport at the electrochemical interface instead of the protonated amino groups thanks to its stronger acidity as well as the structural diffusion mediated by the counter ions ($H_2PO_4^-$).

Introduction

Proton transport in a liquid or a solid medium is a fundamental physicochemical process in many areas of science. For example, in biology, adenosine triphosphate's (ATP) synthesis is driven by the electrochemical potential gradient of protons built up by the proton pumps (complexes I, III, and IV) of the electron transport chain in the inner mitochondrial membrane.[1] With respect to electrochemical energy storage (EES), proton transport decides, to a large extent, how energy storage devices such as batteries operate. Previous reports have pointed out that both the thermodynamically and kinetically accessible proton transport at an electrode-electrolyte interface triggers the co-intercalation of protons with charge carriers more easily even in a near-neutral aqueous electrolyte.[2, 3] This is normally believed to endow aqueous batteries with a higher power density.[4, 5] Notably, whether or not the proton transport at an electrode-electrolyte interface occurs is a result of the inherent properties of both electrode materials (e.g., crystal structure and chemical constitution) and electrolytes (e.g., proton transport mechanism), especially, the latter.[6, 7, 8, 9] Thus, on the basis of proton transport mechanisms in different media, a series of advanced batteries with distinct characteristics have been developed.

In an aqueous medium, the structural diffusion is the most representative proton transport mechanism.[10, 11, 12, 13, 14, 15, 16, 17, 18, 19] It has a more prevalently used term, known as the Grotthuss mechanism. From a modern viewpoint based on the Marcus theory for electron transfer, the initiation of the structural diffusion requires a proton-receiving species presenting a coordination pattern analogous to that of the species into which the proton-receiving species will be transformed after receiving a

proton.[14, 18] As a result, a so-called pre-solvation process, which involves a complicated rearrangement of the local hydrogen bond network around the proton-receiving species to hand a structural defect across one hydrogen bond, is necessary. In other words, the structural diffusion transports a structural defect and its coordination pattern through the fluctuating hydrogen bond network in essence. Copious free protons in the form of the Zundel ($H_5O_2^+$) and Eigen ($H_9O_4^+$) ions are a basic requirement for the structural diffusion.[11, 20, 21] Thus, the structural diffusion becomes more prominent in aqueous inorganic acid solutions with a pH value below 1 and thanks to this feature aqueous acid batteries hold a compelling advantage for rapid EES. Recently, aqueous proton batteries (APBs) as a new class of aqueous acid batteries have been proposed and are characterized by a typical rocking chair mechanism like that of commercial lithium-ion batteries.[22, 23, 24] The electrolytes of APBs, normally being aqueous sulfuric acid or phosphoric acid solutions, only serve as a transmitter of protons without participation in full cell reaction so their energy density is expected to be higher than traditional lead-acid batteries.[25] Despite a fast proton transport enabled by the structural diffusion, a high free proton concentration also elevates the risk of the hydrogen evolution side reaction and renders electrolytes highly corrosive, drawbacks that do not benefit an increase in the operating voltage of APBs and the application of some active materials with inferior resistance to acid corrosion for APBs, either.

Besides the structural diffusion, another proton transport mechanism in an aqueous medium is the vehicular diffusion in which a proton travels a physical distance with its vehicle under an applied electric field.[26] The vehicular diffusion can be described by the Stokes–Einstein equation.[27, 28] Thus, the contributions of the structural ($[H_2O\cdots H\cdots OH_2]^+$) and vehicular diffusions (H_3O^+) to the ionic conductivity of an aqueous phosphoric acid solution are quantified separately through a series of experimental and theoretical approaches.[29] In spite of a slower proton transport in comparison to that via the structural diffusion, one of the characteristics of the vehicular diffusion is that it allows protons to transport in a near-neutral electrolyte environment. For example, ammonia molecules function as a vehicle to carry protons in the form of NH_4^+.[30, 31] However, owing to the extremely strong interaction between an ammonia molecule and a proton, the actual species that undergoes mass transport at an electrode-electrolyte interface is an ammonium ion, that is, the nominal “proton transport” in the bulk phase of an aqueous ammonium salt electrolyte but the “proton transport” at its electrochemical interface not thermodynamically occurring.[3, 30]

Unlike in an aqueous medium, proton transport in a solid medium should more accurately be described as hydrogen ion transport. This is because both a proton and a hydride ion (H^-) serve as a viable charge carrier and topologically travel via a hopping manner.[32, 33, 34, 35] Thus, proton transport mechanisms in a solid medium can be vividly referred to as the hopping diffusion. Among various hydrogen ion conductors, a pioneering one reported by Chen et al., $3CeH_3@BaH_2$ with a core-shell structure, can be used, for the first time, as a solid-state electrolyte for all-solid-state H^- batteries.[36] It shows a H^- conductivity of more than 0.1 mS cm^{-1} and of great significance is that the all-solid-state H^- battery ($CeH_2|3CeH_3@BaH_2|NaAlH_4$) fabricated by it with the rocking chair mechanism delivers an impressive

specific capacity of 984 mAh g^{-1}. It is evident that the acid corrosion from the protons in liquid-state electrolytes is fundamentally solved thanks to the advent of the solid-state H^- conductor. However, a similar liquid-state H^+ conductor with negligible corrosivity and fast proton transport both in its bulk phase and at its electrochemical interface, to our knowledge, is not yet developed.

In this work, inspired by protons' vehicular diffusion, we proposed an amino acid-inorganic acid coupling concept based on which a series of aqueous amino acid salt electrolytes were developed. Amino acids are able to neutralize the free protons from inorganic acids in an aqueous medium by the protonation of their amino group ($-NH_3^+$), resulting in a near-neutral electrolyte environment. Protonated amino acid ions typified by the electromigration of cations transport the protons in the bulk phase via the vehicular diffusion. Their carboxy group with a stronger acidity than the $-NH_3^+$ and solvent water enables the fast proton transport at the electrochemical interface and avoids solvent water taking part in full cell reaction. Such electrolytes render APBs operational not only via the rocking chair mechanism but also in a near-neutral electrolyte environment and thus fill a gap in liquid-state H^+ conductors used for proton batteries.

Results

According to the proposed amino acid-inorganic acid coupling concept, four amino acids were adopted including two nonpolar amino acids, glycine (Gly) and L-proline (L-Pro), and two polar amino acids, L-serine (L-Ser) and L-lysine (L-Lys). With regard to inorganic acids, sulfuric acid (H_2SO_4), hydrochloric acid (HCl), and phosphoric acid (H_3PO_4) were chosen. Subsequently, an orthogonal experiment was conducted. Specifically, the molarity of the different amino acids was all fixed at 1 M and then the variation of the ionic conductivity and the pH value of different amino acid salt electrolytes was recorded by altering the molarity of the inorganic acids at a regular interval. An ionic conductivity of more than 5 mS cm^{-1} and a pH value ranging from 3 to 6 were used as the benchmark to determine whether or not an amino acid salt electrolyte could be employed for near-neutral aqueous proton batteries (NAPBs) characterized by the rocking chair mechanism.[37, 38]

The ionic conductivity of twelve kinds of amino acid salt electrolytes (4 × 3) was shown in **Fig. 1a** and **Supplementary Table 1.**. For the amino acid sulfate and the amino acid hydrochloride electrolytes, their ionic conductivity increases rapidly with inorganic acid concentration. In comparison, the increase in ionic conductivity is relatively moderate for the amino acid phosphate electrolytes due to a lower acidity demonstrated by H_3PO_4. In addition, compared to Gly, L-Pro, and L-Ser, the electrolytes prepared by L-Lys normally have a lower ionic conductivity at the same inorganic acid concentration. All the twelve kinds of amino acid salt electrolytes show an acceptable ionic conductivity of above 7 mS cm^{-1} regardless of the inorganic acid concentration adopted. However, there was a significant difference in the variation of the pH value of these amino acid salt electrolytes (**Fig. 1b** and **Supplementary Table 2.**). First, for the electrolytes prepared by Gly, L-Pro, and L-Ser, the pH values of almost all of them are below 3 except for the one mixed by 1 M Gly and 0.25 M H_3PO_4 with a pH value of 3.04. Second, owing

to a stronger alkalinity shown by L-Lys, the pH value of the L-Lys salt electrolytes fluctuates over a larger range, among which the L-Lys hydrochloride and phosphate electrolytes are much easier to maintain a near-neutral electrolyte environment even at a high inorganic acid concentration of 1.25 M. Thus, the three electrolytes, 1 M Gly + 0.25 H_3PO_4, 1 M L-Lys + 1.25 M HCl (pH = 3.36), and 1 M L-Lys + 1.25 M H_3PO_4 (pH = 3.31), seem to serve as an electrolyte for NAPBs more suitable. On the other hand, in view of a relatively high ionic conductivity (10.5, 57.8, and 18.5 mS cm^{-1}) and a unique effect of the counter ions ($H_2PO_4^-$, this will be discussed later), 1 M L-Lys + 1.25 M H_3PO_4 was eventually selected as the optimum electrolyte.

Then, the coupling behavior of L-Lys and protons was studied by nuclear magnetic resonance (NMR) spectroscopy. **Fig. 1c** shows the ^1H NMR spectra of 1 M L-Lys aqueous solutions with different pH values adjusted through H_3PO_4 or potassium hydroxide (KOH). For L-Lys (**Supplementary Fig. 1**), three active sites are available to couple with protons, including the α amino group (α-NH_2), the ε amino group (ε-NH_2), and the carboxylate group (−COO^-). However, in an aqueous solution, it is hard to identify the labile hydrogen atoms in these groups (α-NH_3^+, ε-NH_3^+, and −COOH) from a ^1H NMR spectrum due to the ultrafast chemical exchange between these labile hydrogen atoms and the ones from water molecules.[39] Fortunately, these labile hydrogen atoms can be indirectly identified by observation of a change in the ^1H chemical shift (δ) of the alkyl groups (−CH_3, −CH_2−, and −CH<) adjacent to these basic groups enabled by the inductive effect of protons. For instance, the change in the ^1H δ of L-Lys's ε methylene group (ε-CH_2) is a good indicator to estimate whether or not the ε-NH_2 is coupled with a proton; similarly, the change in the ^1H δ of L-Lys's α methine group (α-CH) enables analysis of the protonation at the α-NH_2 and the −COO^-.

Hence, the ^1H δ of the ε-CH_2 and the α-CH as a function of pH was further plotted in **Fig. 1d**. For the ε-CH_2, its ^1H δ moves downfield with the decrease of the pH value above the isoelectric point (9.74) but is independent of the pH value below the isoelectric point.[40] This indicates that L-Lys's ε-NH_2 is almost fully protonated at the isoelectric point. Different from that, throughout the pH range studied (11.21 to 2.62), the ^1H δ of the α-CH continuously increases without a sign of tending to be steady. Interestingly, the increase rate of the ^1H δ of the α-CH within a pH range of the isoelectric point to 8.2 is significantly higher than those within other pH ranges (11.21 to the isoelectric point and 8.2 to 2.62). According to the above results, three key conclusions can be drawn. First, L-Lys's α-NH_2 can also be protonated above the isoelectric point, however, owing to its weaker alkalinity compared to the ε-NH_2, it cannot be fully protonated until the pH value reaches 8.2. Such a conclusion is further confirmed by the evolution of the ^1H δ of the β-CH_2. Second, the −COO^- starts to bind a proton from the isoelectric point downward. Thus, the steep increase in the ^1H δ of the α-CH is observed within the isoelectric point to 8.2 because of the simultaneous protonation at the α-NH_2 and the −COO^-. Third, L-Lys's −COOH is a stronger Brønsted acid than solvent water so the −COO^- cannot be fully protonated even at a pH value of 2.62. Based on the pK_a

of L-Lys's −COOH, about 0.07 M $-COO^-$ exists in the form of its conjugate acid at a pH value of 3.31 (1 M L-Lys + 1.25 M H_3PO_4).

In addition, the coupling behavior of L-Lys and protons as revealed by NMR spectroscopy could also be evidenced by the DFT calculations. **Fig. 1e** shows the Gibbs free energy diagram of a L-Lys anion being protonated step by step. Among the three basic groups, the ε-NH_2 is the most favorable to bind a proton in energetics, followed by the α-NH_2 and the $-COO^-$. Notably, the L-Lys anion binding a proton at the ε-NH_2 or the α-NH_2 has a similar Δ*G* value (−16.14 versus −16.00 kcal mol^{-1}). It explains why both the ε-NH_2 and the α-NH_2 start to bind a proton at a pH value as high as 11.21. Overall, the L-Lys phosphate electrolyte, 1 M L-Lys + 1.25 M H_3PO_4, with a pH value of 3.31 was a feasible electrolyte for NAPBs, where the protonated L-Lys ions are positively charged and are able to transport the protons in the bulk phase via the vehicular mechanism.

Subsequently, as a proof of concept, an orthorhombic molybdenum oxide (α-MoO_3) single crystal was chosen as the model material and its electrochemical behavior was investigated in the above electrolyte. The α-MoO_3 single crystal used in this work was synthesized via a hydrothermal method. It has a layered crystal structure and a ribbonlike crystal morphology with the feature of a large aspect ratio (**Supplementary Fig. 2-4**). The terminal oxygen (O_t) in its interlayer and the asymmetric oxygen (O_a) that bonds with two molybdenum ions along the *a* direction in its intralayer form several pathways that allow migration for protons (**Supplementary Fig. 5**).[41, 42]

Fig. 2a and **2b** show the galvanostatic charge-discharge (GCD) curves of the first three cycles at 0.5 C (1 C = 372 mA g^{-1}) and the corresponding dQ/dV curves, respectively. Significant electrochemical activity is observed for the α-MoO_3 electrode, as reflected by the two potential platforms and the four pairs of redox peaks of the reversible cycles. It delivers an initial discharge capacity of 372 mAh g^{-1} and a reversible charge capacity of 183 mAh g^{-1} at 0.5 C (**Fig. 2c** and **2d**). As the current density increases to 40 C, a specific capacity of 84 mAh g^{-1} remains corresponding to a rate capability of 46% versus 0.5 C. An initial capacity retention of 76% is achieved over 1000 GCD cycles at 20 C (**Fig. 2e**). The electrochemical properties of the α-MoO_3 electrode were also studied in a 1 M L-Lys aqueous electrolyte and in a 1.25 M H_3PO_4 aqueous electrolyte for comparison. No significant electrochemical activity is demonstrated by the α-MoO_3 electrode in 1 M L-Lys (**Supplementary Fig. 6**). By contrast, the electrochemical behavior of the α-MoO_3 electrode in 1.25 M H_3PO_4 is highly similar to that in 1 M L-Lys + 1.25 M H_3PO_4 (**Supplementary Fig. 7**). Different from the L-Lys phosphate electrolyte, a higher electrode potential is observed in 1.25 M H_3PO_4, which is in accordance with the tendency predicted via the Nernst equation (**Supplementary Fig. 8**). Moreover, kinetics analysis using the Randles–Ševčík and the Dahms–Ruff equations shows that the electrochemical reactions of the α-MoO_3 electrode in the L-Lys phosphate electrolyte have homogeneous electron self-exchange rate constants between 0.393 and 2.521×10^6 mol^{-1} m^3 s^{-1} which are close to or even higher than those of reversible proton storage

reactions (**Supplementary Fig. 9**, **Supplementary Table 3.**, and **Supplementary Note 1**).[43, 44, 45] Thus, the above electrochemical results preliminarily confirm that the L-Lys phosphate electrolyte enables reversible proton storage in the α-MoO_3 electrode.

Then, the evolution of the crystal structure of the α-MoO_3 electrode during the initial cycle was analyzed in the L-Lys phosphate electrolyte via *ex-situ* X-ray diffractometry (XRD).[43, 46, 47] The selected states of charge (SOC) were highlighted in **Fig. 3a**. As the polarization potential decreases from open circuit potential (OCP) to b ($H_{0.3}MoO_3$) (**Fig. 3b** and **3c**), a two-phase reaction occurs with the orthorhombic α-MoO_3 transforming into the orthorhombic hydrogen molybdenum bronze (HMB) I phase (H_xMoO_3, 0.23 < x < 0.4, **Supplementary Fig. 10**). From b to c ($H_{0.6}MoO_3$), a new phase is detected corresponding to the HMB II phase (H_xMoO_3, 0.85 < x < 1.04, **Supplementary Fig. 11**). As the electrode is further discharged to d (H_1MoO_3), the HMB I and II phases still exist, however another new phase, which corresponds to the HMB III phase (H_xMoO_3, 1.55 < x < 1.72, **Supplementary Fig. 12**), emerges. Almost all the HMB I and II phases transform into the HMB III phase at e ($H_{1.6}MoO_3$) so the electrochemical reaction from e to g (H_2MoO_3) is mainly attributed to the solid-solution reaction of the HMB III phase (**Supplementary Fig. 13**). During the initial charge process, both the solid-solution reaction of the HMB III phase (g to h) and the two-phase reaction from the HMB III to II phases (h to k) are reversible (**Supplementary Fig. 13**). Not only that, but the electrochemical reaction from k to l, related to the solid-solution reaction of the HMB II phase, is reversible, too. Note that the evolution of the *d*-spacing of the (020) plane is always less than 5% during the whole initial cycle, indicative of the electrochemical reactions only bare protons take part in (**Fig. 3c**).[48]

The occupancy of protons was also studied using *ex-situ* Fourier transform infrared spectroscopy (FTIR). As **Fig. 3d** shows, no characteristic peaks of L-Lys are detected from all the FTIR spectra, again demonstrating such electrochemical reactions that only involve protons. The zoomed-in FTIR spectra within a wavenumber range of 1100 to 700 cm^{-1} was further shown in **Fig. 3e** where the spectral band with a wavenumber of 996 cm^{-1} at the OCP is assigned to the $\nu(Mo{=}O_t)$ of α-MoO_3.[49] It blue-shifts to 1005 cm^{-1} at b, suggesting a slight shrinkage in the $Mo{=}O_t$ bond of the HMB I phase.[50] As the electrode is discharged to c at which the HMB II phase emerges, two new spectral bands are probed. One with a higher wavenumber of 987 cm^{-1} is assigned to the $\nu(Mo{=}O_t)$ from a $Mo{=}O_t{-}H\cdots O_t$ motif; the other one with a lower wavenumber of 950 cm^{-1} is related to the $\nu(Mo{=}O_t)$ from a $Mo{=}O_t{<}H_2\cdots O_t$ motif. This implies that most of protons occupy the intralayer sites (the 8h site in the *Cmcm* space group) and bond with the O_a in the HMB I phase, however, for the HMB II phase protons can further occupy the interlayer sites in the forms of a single proton or a proton pair (the 4i or 8j site in the *C2/m* space group) bonding with the O_t (**Fig. 3f**).[51, 52, 53, 54] On the other hand, at the SOCs of e to g, only the spectral band at 950 cm^{-1} is detected, suggesting that the occupancy of the protons at the interlayer sites is almost in the form of the proton pair in the HMB III phase (**Fig. 3f**).[53, 54] The same conclusion can also be drawn from the FTIR spectra of the initial charge process. Thus, the diffractometry and spectroscopy results

unambiguously demonstrate the reversible proton storage of the α-MoO_3 electrode in the L-Lys phosphate electrolyte.

In-situ attenuated total reflection surface-enhanced infrared absorption spectroscopy (ATR-SEIRAS) and *in-situ* surface-enhanced Raman spectroscopy (SERS) were employed to yield a clear mechanistic picture for the proton transport behavior at the electrode-electrolyte interface. As shown in **Fig. 4a** and **4b**, the spectral bands at 1679, 1535, and 1355 $cm^{-1}$are attributed to the *v*(C=O) of the −COOH and the $v_{as}(CO_2)$ and $v_s(CO_2)$ of the $-COO^-$, respectively.[55, 56] The intensity of the *v*(C=O) gradually increases below −0.2 V and then remains almost unchanged above −0.2 V during the charge process. By contrast, the variation of the *v*(C=O) in intensity is reversed during the discharge process, that is, being stable above −0.2 V but being gradually attenuated below −0.2 V. It demonstrates that the −COOH and the $-COO^-$ of the protonated L-Lys ions are the sites responsible for transporting protons at the interface. In addition, the *in-situ* pH monitoring at the interface was conducted to further verify this conclusion. As shown in **Fig. 4c**, the variation of the pH value is not significant during both the charge and discharge processes, however, there is a pH jump (3.1 to 3.4) once the direction of current is switched. According to the Henderson−Hasselbalch equation,[57] about 5 mol% of the −COOH will transfer into the $-COO^-$ in contrast to a change of 0.08 mol‰ for $H_2PO_4^{2-}$ to HPO_4^- if the pH value increases from 3.1 to 3.4 (**Supplementary Note 2**). In other words, the −COOH/$-COO^-$ couple enables the fast proton transport at the interface by instantaneously regulating the molar ratio of itself with an extremely low barrier in thermodynamics. Moreover, this result also proves that the counter ion, $H_2PO_4^{2-}$, has few contributions to the proton storage of the α-MoO_3 electrode. The *in-situ* SERS spectra further show that the characteristic peaks ($v_{as}(NH_3)$ of the $-NH_3^+$ at 2975 cm^{-1}, $v_{as}(CH_2)$ of the $-CH_2-$ at 2940 cm^{-1}, and $v_s(CH_2)$ of the $-CH_2-$ at 2877 cm^{-1}, **Supplementary Fig. 14**) of the protonated L-Lys ions remain stable in intensity over the entire course of the electrochemical measurement, suggestive of the steady-state proton transport at the interface (**Fig. 4d** and **4e**).[58]

Despite the few contributions of proton storage from $H_2PO_4^-$, we found that it significantly influences the rate capability of the electrode. As shown in **Fig. 4f** to **4h**, in 1 M L-Lys + 1.25 M HCl which shows a similar pH value (3.36) but a higher ionic conductivity (57.8 mS cm^{-1}) compared to 1 M L-Lys + 1.25 M H_3PO_4, the α-MoO_3 electrode delivers a reversible charge capacity of 186 mAh g^{-1} at 0.5 C, a rate capability of 25% at 40 C versus 0.5 C, and an initial capacity retention of 18% over 1000 GCD cycles at 20 C. It suggests that in an amino acid salt electrolyte the rate-determining step of the proton storage of electrode materials is governed by the proton transport at the interface rather than in the bulk phase. Thus, we further compared the IRAS spectra of the L-Lys phosphate electrolyte at the interface and in the bulk phase to provide greater insight into the correlation of the proton transport at the interface with $H_2PO_4^-$. The former was extracted from the data of the *in-situ* ATR-SEIRAS experiment (**Fig. 4a**) and meanwhile the IRAS spectra of 1 M KH_2PO_4 and 1 M K_2HPO_4 aqueous solutions were also involved as a reference.

As shown in **Fig. 4i**, a set of spectral bands are identified at 1160 and 1077 cm^{-1}, corresponding to the $v_{as}(PO_2)$ and $v_s(PO_2)$ of $H_2PO_4^-$ ions in the bulk phase of the L-Lys phosphate electrolyte,[59] respectively. For the one at the interface, the highly similar spectral bands are also detected, however, with a slight blue-shift that could be related to the Stark effect;[60] besides, a new peak at 1288 cm^{-1} and a significant enhancement in absorbance within a wavenumber range of 1140 to 1100 cm^{-1} are observed and are assigned to the δ(P–O–H···O–P) of $(H_xPO_4^{x-3})_n$ (x = 2, 3, or 4) aggregates[61] and the vibrational modes of $H_4PO_4^+$ ions simulated through the DFT calculations (**Supplementary Fig. 15** , **16**). It should be noted that the former periodically varies in absorbance during the charge and discharge processes and a similar trend is also observed for the shoulder peak (marked by a red dashed box) close to it with a barely discernible absorbance (**Fig. 4b** and **4i)**. Moreover, another component representing the v(P=O) of H_3PO_4 molecules at 1180 cm^{-1} is also identified via the Gaussian fit of the spectrum (interface, 0 V) ranging from 1250 to 1025 cm^{-1} (**Supplementary Fig. 17**).[59] A previous study reported by Kreuer et al. suggests that in neat liquid H_3PO_4 its superior proton conductivity originates from the extended Grotthuss chains formed by the $(H_xPO_4^{x-3})_n$ aggregates.[62] These extended Grotthuss chains with a strong but frustrated hydrogen bond network enable fast intramolecular proton transport via the structural diffusion driven by a hydrogen bond rearrangement. In our case, although the hydrogen bond network built up by H_2O is interrupted at the interface from the disturbance of the protonated L-Lys ions (**Fig. 4j**),[63] a new pathway established by the $(H_xPO_4^{x-3})_n$ aggregates is made accessible. This allows the fast proton transport at the interface via the structural diffusion by dynamically adjusting the hydrogen bond network of the $(H_xPO_4^{x-3})_n$ aggregate themselves and the one of the surrounding environments around them, which can be proved by the periodic variation of the absorbance of the δ(P–O–H···O–P) and its shoulder peak as mentioned earlier.

Lastly, the universality of such an electrolyte for aqueous proton batteries was further verified by testing a small molecule quinone cathode, tetrachloro-1,4-benzoquinone (TCBQ), in it, whose electrochemical behavior is still dominated by proton storage (**Supplementary Fig. 18**-**20**). In addition, a NAPB was fabricated by using a protonated α-MoO_3 anode (H_2MoO_3), the L-Lys phosphate electrolyte, and a TCBQ cathode (**Supplementary Fig. 21**). It delivers a specific capacity of 181 mAh g^{-1} and an energy density of 83 Wh kg^{-1} (based on the mass loading of the anode). According to the disclosed proton transport mechanisms, the electrochemical processes of the device operating are described as follows,

Anode: $H_2MoO_3 - e^- + NH_3^+(CH_2)_4(NH_3^+)COO^- \leftrightarrow HMoO_3 + NH_3^+(CH_2)_4(NH_3^+)COOH$,

Cathode: $C_6Cl_4O_2 + 2e^- + 2NH_3^+(CH_2)_4(NH_3^+)COOH \leftrightarrow C_6Cl_4(OH)_2 + 2NH_3^+(CH_2)_4(NH_3^+)COO^-$,

Full cell: $2H_2MoO_3 + C_6Cl_4O_2 \leftrightarrow 2HMoO_3 + C_6Cl_4(OH)_2$.

Discussion

Aqueous amino acid salt solutions were proposed for the first time as an electrolyte for aqueous proton batteries (APBs). Among them, the aqueous L-Lys phosphate solution (1 M L-Lys + 1.25 M H_3PO_4) with both a high ionic conductivity and a suitable pH value was screened as the optimum one. In its bulk phase, the free protons from H_3PO_4 are captured by L-Lys molecules via the protonation at their α-NH_2 and ε-NH_2 groups; as a result, a near-neutral electrolyte environment is formed and the resulting L-Lys ions being positively charged transport protons via the vehicular diffusion. Its feasibility as an electrolyte for APBs was further demonstrated by testing the metal oxide anode (α-MoO_3) and the small molecule quinone cathode (TCBQ) in it, both of which exhibit typical proton storage behavior. The *in-situ* spectroscopy results reveal that the –COOH/–COO^- couple is the sites responsible for the proton transport at the electrode-electrolyte interface. In addition, the chemical constitution at the interface can significantly impact the proton mobility across it. The counter ions, $H_2PO_4^-$, are spontaneously assembled into hydrogen-bonded $(H_xPO_4^{x-3})_n$ aggregates at the interface during the electrochemical processes. These aggregates serve as the extended Grotthuss chains and accelerate the proton mobility across the interface via the structural diffusion. Thus, compared to the L-Lys hydrochloride electrolyte, the electrodes in the above electrolyte show a better rate capability even with a lower ionic conductivity. The aqueous proton battery (H_2MoO_3|L-Lys^+·$H_2PO_4^-$|TCBQ) was fabricated using this electrolyte. It operates not only via the rocking chair mechanism but also in a near-neutral electrolyte environment and delivers a specific capacity of 181 mAh g^{-1} and an energy density of 83 Wh kg^{-1}.

Methods

Reagents and Materials

Graphite foil (F02510Z) was purchased from SGL Carbon (Germany). Poly(vinylidene fluoride) (PVDF, Solef 5130) was purchased from Solvay Pharmaceuticals Co., Ltd. (France). Aqueous polytetrafluoroethylene (PTFE, 60 wt%, D-210C) dispersion was purchased from Daikin Industries, Ltd. (Japan). Ketjenblack (ECP-600JD) was purchased from Lion Specialty Chemicals Co., Ltd. (Japan). HNO_3 (65 wt%, AR), H_2SO_4 (98wt%, AR), HCl (37 wt%, AR), KOH (AR), and N-Methyl-2-pyrrolidone (NMP, AR) were purchased from Tianjin Komiou Chemical Reagent Co., Ltd. (PR China). H_3PO_4 (85 wt%, GR), glycine (99%), L-proline (99%), L-serine (99%), L-lysine (99%), $(NH_4)_6Mo_7O_{24}·4H_2O$ (AR), and tetrachloro-1,4-benzoquinone (TCBQ, 98%) were purchased from Aladdin Chemical Reagent Co., Ltd. (PR China). KCl (GR) and absolute ethanol (AR) were purchased from Sinopharm Chemical Reagent Co., Ltd. (PR China). High-purity N_2 (99.999%) was purchased from Dalian Kerui Gas Co., Ltd.

Synthesis of α-MoO_3 Single Crystal

2 g $(NH_4)_6Mo_7O_{24}·4H_2O$ was dissolved in 50 mL deionized water, and then 10 mL 65 wt% HNO_3 was added. After stirring for 20 min, a transparent solution was obtained and then transferred into a 100 ml

Teflon-lined stainless-steel autoclave. The autoclave was heated at 200 °C for 24 h in an electric forced air-drying oven. The obtained powder was alternately washed with deionized water and absolute ethanol and collected via centrifugation. A α-MoO_3 single crystal was eventually obtained after the drying of the wet powder under vacuum at 60 °C for 12 h.

Preparation of α-MoO_3 Electrodes

The α-MoO_3 single crystal, PVDF, and Ketjenblack was first mixed at a weight ratio of 7:2:1. Then, NMP was added into the above mixture to form homogeneous slurry after grinding; a α-MoO_3 electrode was prepared by casting the slurry onto a graphite foil. Last, the α-MoO_3 electrode was dried under vacuum at 60 °C for 12 h to remove residual NMP.

Preparation of TCBQ Electrodes

Commercially available TCBQ was first mixed with Ketjenblack and then aqueous PTFE dispersion with a dilute mass fraction of 10% was added. The weight ratio of the three was 5:4:1. Homogeneous slurry was obtained after grinding. A TCBQ electrode was prepared by drop-casting the slurry onto a graphite foil. The TCBQ electrode was dried under vacuum at 60 °C for 12 h to remove residual water.

***In-Situ* ATR-SEIRAS Measurements**

In-situ ATR-SEIRAS measurements were carried out in a homemade spectro-electrochemical cell with a hemicylindrical Si prism whose surface was chemically plated with an Au film, a Pt wire, and a saturated calomel electrode (SCE) as the working electrode, the counter electrode, and the reference electrode, respectively. Dilute α-MoO_3 dispersion made by a method similar to that in Section 1.3 was drop-cast onto the surface of the working electrode to form an ultrathin α-MoO_3 coating. A Fourier transform infrared spectrometer (Thermo Fisher Scientific, Nicolet iS50, USA) equipped with a liquid nitrogen-cooled MCT-B detector was employed for *in-situ* ATR-SEIRAS measurements. Infrared spectra were acquired over a wavenumber range of 4000 to 1000 cm^{-1}, with a spectral resolution of 4 cm^{-1}, at a time interval of 20 s, and by averaging 32 scans and were expressed using an absorbance unit (A), which is defined as $A = -\log R/R_0$, where R and R_0 are the intensity of reflected radiation at a state of charge and the one at open circuit potential, respectively. The angle of incidence was set at 60 degrees. During the whole electrochemical process, high-purity N_2 (99.999%) with a constant flow rate was injected into the optical path to purge the air in it.

***In-Situ* SERS Measurements**

In-situ SERS measurements were conducted in a homemade spectro-electrochemical cell. An Au electrode with an electrochemically roughed surface was used as the working electrode. Dilute α-MoO_3 dispersion was drop-cast onto its surface to form an ultrathin α-MoO_3 coating. The obtained electrode was placed behind the sapphire window with a thick of 0.5 mm. A Pt wire and a SCE were employed as the counter electrode and the reference electrode, respectively. Raman spectra were collected in a range

of 3500 to 2700 cm^{-1} using a customized confocal Raman spectrometer (HORIBA Jobin Yvon, LabRAM HR800, Japan) equipped with an 18 mW He:Ne 633 nm laser source for excitation, a 600 lines/mm grating to disperse scattering light, and a long working distance objective lens (Nikon, 50x/0.45 NA, Japan) to focus the laser beam on the surface of the working electrode and collect the resulting scattering light. The laser power was set at 1.8 mW. The integral time was set at 25 s with 2 accumulations.

Characterization

The ionic conductivity and the pH value of different amino acid salt electrolytes were measured by a conductivity meter (REX, DDBJ-350F, PR China) and a high-precision pH meter (METTLER TOLEDO, SD20, Switzerland), respectively. The ^{1}H NMR spectra of 1 M L-lysine aqueous solutions with different pH values were collected on a nuclear magnetic resonance spectrometer (Bruker, AVANCE III 400 MHz, Switzerland) using a standard single-pulse sequence and calibrated to 2,2-dimethyl-2-silapentane-5-sulfonate sodium salt (DSS) at 0 ppm. To avoid the direct contact of a reference solution of DSS in D_2O used for field-frequency lock and ^{1}H NMR spectrum calibration with samples, a coaxial NMR tube was employed with the inner capillary filled with the reference solution and the outer tube filled with a sample.

The crystal structure of the α-MoO_3 single crystal and the evolution of its crystal structure during charge and discharge processes were analyzed through an X-ray powder diffractometer (XRD, Malvern Panalytical, Empyrean, Netherlands) operating with Cu Kα radiation using a voltage of 40 kV and a current of 40 mA. Rietveld refinement was conducted by the GSAS-II software. Its morphology and microstructure were further observed using a scanning electron microscope at an accelerating voltage of 5 kV (SEM, JEOL, JSM-7800F, Japan) and a transmission electron microscopy at an accelerating voltage of 200 kV (TEM, JEOL, JEM-2100, Japan). High-angle annular dark-field scanning transmission microscopy (HAADF-STEM) imaging and integrated differential phase contrast scanning transmission electron microscopy (iDPC-STEM) imaging were performed on an aberration-corrected scanning transmission electron microscope (Thermo Fisher Scientific, Titan Cubed Themis G2300, USA) at an accelerating voltage of 300 kV. All *ex-situ* FTIR spectra were acquired on a Fourier transform infrared spectrometer (Thermo Fisher Scientific, Nicolet 6700, USA) over a wavenumber range of 4000 to 400 cm^{-1}, at a spectral resolution of 4 cm^{-1}, and by averaging 32 scans.

All electrochemical measurements were conducted on a multichannel analyzer (BioLogic, VSP-3e, France). A commercially available three-electrode cell (Aida, C002 30 mL, RP China) was employed for electrochemical measurements using a piece of graphite foil and a SCE as the counter electrode and the reference electrode, respectively.

DFT Calculations

All DFT calculations were carried out using the B3LYP functional by the Gaussian 16 A.03 software.[64] The 6-311+G(d,p) basis set was adopted for the geometry optimization and frequency calculations of all atoms.[65, 66, 67] Moreover, the long-range dispersion interaction in a molecule or an ion was also taken into our DFT calculations by using the Grimme's D3 dispersion correction with the Becke–Johnson damping (Grimme's D3(BJ)).[68, 69] Water was selected as the solvent for the DFT calculations and thus its solvation effect was described using the Solvation Model Based on Density (SMD) implicit solvation model.[70] Analysis on wave functions was conducted by the Multiwfn 3.8(dev) code.[71, 72] The Gibbs free energies of L-lysine molecules or ions formed by the protonation of an L-lysine anion with different numbers of protons (1, 2, and 3) or at the different basic groups (α-NH_2, ε-NH_2, and $-COO^-$) were calculated by the equation as follows,

$$G = E + E_{ZPE} - TS \quad \cdots\cdots\cdots\cdots\cdots\cdots\cdots\cdots\cdots\cdots \text{Equation 1,}$$

where E, E_{ZPE}, T, and S were DFT energy, zero-point energy, absolute temperature (298.15 K), and entropy, respectively. The electrostatic potential (ESP) extremum on the van der Waals surface projection of an L-lysine anion was confirmed by quantitative analysis on its ESP surface using the Multiwfn 3.8(dev) code[73] and the isosurface map of its ESP was further rendered by the VMD visualization program using the file exported from the Multiwfn 3.8(dev) code.[74] A correction factor of 0.9688 was applied to the fundamental frequency of the vibrational modes of $H_2PO_4^-$ and $H_4PO_4^+$ simulated via the DFT calculations.

Data Availability

The data supporting the findings of the study are included in the main text and supplementary information files. Source data are provided with this paper.

Declarations

Competing Interests

The authors declare no competing financial interest.

References

1. Allen JF. Photosynthesis of ATP—Electrons, Proton Pumps, Rotors, and Poise. *Cell* **110**, 273–276 (2002).
2. Wang W, Balland V, Branca M, Limoges B. A Unified Charge Storage Mechanism to Rationalize the Electrochemical Behavior of Quinone-Based Organic Electrodes in Aqueous Rechargeable Batteries. *J.Am.Chem.Soc.* **146**, 15230–15250 (2024).

3. Nan J, You Y, Zha W, Xia L, Ruan Q, Sun Z. Light-Induced NH_4^+ Deprotonation Drives NH_4^+/H^+ Hybrid Storage Toward Near-Theoretical Capacity in $NH_4V_4O_{10}$ Electrodes. *J.Am.Chem.Soc.* **148**, 1347–1355 (2026).
4. Sun T, Nian Q, Ren X, Tao Z. Hydrogen-bond chemistry in rechargeable batteries. *Joule* **7**, 2700–2731 (2023).
5. Li W*, et al.* Proton Storage Chemistry in Aqueous Zinc-Inorganic Batteries with Moderate Electrolytes. *Adv. Mater.* **37**, No. 2414019 (2025).
6. Sun Z*, et al.* Heterointerface Built Up by Ultrathin Amorphous MoO_3 Conformal Coating Enables $V_5O_{12}{\cdot}6H_2O$ with Superior Properties for Aqueous Zinc Batteries. *Nano Lett.* **25**, 1373–1380 (2025).
7. Li S*, et al.* Unraveling the "Gap-Filling" Mechanism of Multiple Charge Carriers in Aqueous Zn-MoS_2 Batteries. *Angew. Chem. Int. Ed.* **63**, No. e202320075 (2024).
8. Blanc LE, Kundu D, Nazar LF. Scientific Challenges for the Implementation of Zn-Ion Batteries. *Joule* **4**, 771–799 (2020).
9. Li C, Kingsbury R, Zhou L, Shyamsunder A, Persson KA, Nazar LF. Tuning the Solvation Structure in Aqueous Zinc Batteries to Maximize Zn-Ion Intercalation and Optimize Dendrite-Free Zinc Plating. *ACS Energy Lett.* **7**, 533–540 (2022).
10. Flór M*, et al.* Dissecting the hydrogen bond network of water: Charge transfer and nuclear quantum effects. *Science* **386**, No. eads4369 (2024).
11. Thämer M, De Marco L, Ramasesha K, Mandal A, Tokmakoff A. Ultrafast 2D IR spectroscopy of the excess proton in liquid water. *Science* **350**, 78–82 (2015).
12. Woutersen S, Bakker HJ. Ultrafast Vibrational and Structural Dynamics of the Proton in Liquid Water. *Phys. Rev. Lett.* **96**, No. 138305 (2006).
13. Markovitch O, Chen H, Izvekov S, Paesani F, Voth GA, Agmon N. Special Pair Dance and Partner Selection: Elementary Steps in Proton Transport in Liquid Water. *J. Phys. Chem. B* **112**, 9456–9466 (2008).
14. Agmon N. The Grotthuss mechanism. *Chem. Phys. Lett.* **244**, 456–462 (1995).
15. Tuckerman ME, Marx D, Klein ML, Parrinello M. On the Quantum Nature of the Shared Proton in Hydrogen Bonds. *Science* **275**, 817–820 (1997).
16. Marx D, Tuckerman ME, Hutter J, Parrinello M. The nature of the hydrated excess proton in water. *Nature* **397**, 601–604 (1999).
17. Vuilleumier R, Borgis D. Transport and spectroscopy of the hydrated proton: A molecular dynamics study. *J. Chem. Phys.* **111**, 4251–4266 (1999).
18. Schmitt UW, Voth GA. The computer simulation of proton transport in water. *J. Chem. Phys.* **111**, 9361–9381 (1999).
19. Berkelbach TC, Lee H-S, Tuckerman ME. Concerted Hydrogen-Bond Dynamics in the Transport Mechanism of the Hydrated Proton: A First-Principles Molecular Dynamics Study. *Phys. Rev. Lett.* **103**, No. 238302 (2009).

20. Tian Y*, et al.* Visualizing Eigen/Zundel cations and their interconversion in monolayer water on metal surfaces. *Science* **377**, 315–319 (2022).
21. Zhu B-Q, Zhang C-Y, Zhen E-F, Zhao D-C, Cai J, Chen Y-X. Proton Accumulation near the Au Electrode/Acid Interface Probed by Electrochemical In Situ Infrared Spectroscopy. *J. Phys. Chem. C* **129**, 11958–11966 (2025).
22. Cai H*, et al.* Isotope interface design for high-energy aqueous proton batteries. *Chem* **11**, No. 102551 (2025).
23. Wu X*, et al.* Diffusion-free Grotthuss topochemistry for high-rate and long-life proton batteries. *Nat. Energy* **4**, 123–130 (2019).
24. Guyomard D, Tarascon J-M. Rocking-chair or lithium-ion rechargeable lithium batteries. *Adv. Mater.* **6**, 408–412 (1994).
25. Lopes PP, Stamenkovic VR. Past, present, and future of lead–acid batteries. *Science* **369**, 923–924 (2020).
26. Kreuer K-D, Rabenau A, Weppner W. Vehicle Mechanism, A New Model for the Interpretation of the Conductivity of Fast Proton Conductors. *Angew. Chem. Int. Ed.* **21**, 208–209 (1982).
27. Batchelor GK. Brownian diffusion of particles with hydrodynamic interaction. *J. Fluid Mech.* **74**, 1–29 (1976).
28. Verma AK, Thorat AS, Shah JK. Estimating ionic conductivity of ionic liquids: Nernst–Einstein and Einstein formalisms. *J. Lon. Liq.* **4**, No. 100089 (2024).
29. Li Z*, et al.* Quantitative and mechanistic insights into proton dynamics for fast energy storage. *Nat. Mater.* **24**, 1968–1977 (2025).
30. Wu X, Qi Y, Hong JJ, Li Z, Hernandez AS, Ji X. Rocking-Chair Ammonium-Ion Battery: A Highly Reversible Aqueous Energy Storage System. *Angew. Chem. Int. Ed.* **56**, 13026–13030 (2017).
31. Huang X, Xu J, Xu X, Wang S. Improved Near-Neutral Hydrogen Evolution Reaction Kinetics through Electrolyte Engineering with the Efficient Hydrogen Source NH_4^+. *ACS Catal.* **14**, 14606–14621 (2024).
32. Hirose T*, et al.* High-capacity, reversible hydrogen storage using H^--conducting solid electrolytes. *Science* **389**, 1252–1255 (2025).
33. Lim D-W, Kitagawa H. Proton Transport in Metal–Organic Frameworks. *Chem. Rev.* **120**, 8416–8467 (2020).
34. Mauritz KA, Moore RB. State of Understanding of Nafion. *Chem. Rev.* **104**, 4535–4586 (2004).
35. Kreuer K-D, Paddison SJ, Spohr E, Schuster M. Transport in Proton Conductors for Fuel-Cell Applications: Simulations, Elementary Reactions, and Phenomenology. *Chem. Rev.* **104**, 4637–4678 (2004).
36. Cui J*, et al.* A room temperature rechargeable all-solid-state hydride ion battery. *Nature* **646**, 338–342 (2025).

37. Xu K. Nonaqueous Liquid Electrolytes for Lithium-Based Rechargeable Batteries. *Chem. Rev.* **104**, 4303–4418 (2004).
38. Tan J, Liu J. Electrolyte Engineering Toward High-Voltage Aqueous Energy Storage Devices. *Energy Environ. Mater.* **4**, 302–306 (2021).
39. Lambert JB, Mazzola EP, Ridge CD. *Nuclear magnetic resonance spectroscopy: an introduction to principles, applications, and experimental methods*. (John Wiley & Sons, Hoboken, New Jersey, 2019).
40. Nelson DL, Cox MM. *Lehninger Principles of Biochemistry*. (W.H. Freeman, New York, New York, 2005).
41. Brezesinski T, Wang J, Tolbert SH, Dunn B. Ordered mesoporous α-MoO_3 with iso-oriented nanocrystalline walls for thin-film pseudocapacitors. *Nat. Mater.* **9**, 146–151 (2010).
42. Kim H-S*, et al.* Oxygen vacancies enhance pseudocapacitive charge storage properties of MoO_{3-x}. *Nat. Mater.* **16**, 454–460 (2017).
43. Cai X, Tang S, An Z-m, Shao Q, Zhang K, Liu H. Stable proton storage in α-MoO_3 via a bifunctional molecular crowding electrolyte. *Electrochim. Acta* **542**, No. 147456 (2025).
44. Ma T*, et al.* Understanding the mechanism of a conjugated ladder polymer as a stable anode for acidic polymer-air batteries. *Joule* **7**, 2261–2273 (2023).
45. Wang R*, et al.* A Long-Range Planar Polymer with Efficient π-Electron Delocalization for Superior Proton Storage. *Adv. Mater.* **36**, No. 2402681 (2024).
46. Guo H*, et al.* Two-Phase Electrochemical Proton Transport and Storage in α-MoO_3 for Proton Batteries. *Cell Rep. Phys. Sci.* **1**, No. 100225 (2020).
47. Wang C*, et al.* Suppressed Dissolution and Enhanced Desolvation in Core–Shell MoO_3@TiO_2 Nanorods as a High-Rate and Long-Life Anode Material for Proton Batteries. *Adv. Energy Mater.* **12**, No. 2200157 (2022).
48. Ma Z, Shi X-M, Nishimura S-i, Ko S, Okubo M, Yamada A. Anhydrous Fast Proton Transport Boosted by the Hydrogen Bond Network in a Dense Oxide-Ion Array of α-MoO_3. *Adv. Mater.* **34**, No. 2203335 (2022).
49. Mai LQ*, et al.* Lithiated MoO_3 Nanobelts with Greatly Improved Performance for Lithium Batteries. *Adv. Mater.* **19**, 3712–3716 (2007).
50. Sha X, Chen L, Cooper AC, Pez GP, Cheng H. Hydrogen Absorption and Diffusion in Bulk α-MoO_3. *J. Phys. Chem. C* **113**, 11399–11407 (2009).
51. Rousseau R, Canadell E, Alemany P, Galván DH, Hoffmann R. Origin of the Metal-to-Insulator Transition in $H_{0.33}MoO_3$. *Inorg. Chem* **36**, 4627–4632 (1997).
52. Adams S, Moretzki O, Canadell E. Global instability index optimizations for the localization of mobile protons. *Solid State Ion.* **168**, 281–290 (2004).
53. Braïda B, Adams S, Canadell E. Concerning the Structure of Hydrogen Molybdenum Bronze Phase III. A Combined Theoretical–Experimental Study. *Chem. Mater.* **17**, 5957–5969 (2005).

54. Ritter C, Müller-Warmuth W, Schöllhorn R. Structure and motion of hydrogen in molybdenum bronzes H_xMoO_3 as studied by nuclear magnetic resonance. *J. Chem. Phys.* **83**, 6130–6138 (1985).
55. A. Mohamed W*, et al.* Engineering Porosity and Functionality in a Robust Twofold Interpenetrated Bismuth-Based MOF: Toward a Porous, Stable, and Photoactive Material. *J.Am.Chem.Soc.* **146**, 13113–13125 (2024).
56. Firet NJ, Smith WA. Probing the Reaction Mechanism of CO_2 Electroreduction over Ag Films via Operando Infrared Spectroscopy. *ACS Catal.* **7**, 606–612 (2017).
57. Huang J*, et al.* Tracking interfacial single-molecule pH and binding dynamics via vibrational spectroscopy. *Sci. Adv.* **7**, No. abj1790 (2021).
58. Snyder RG. Vibrational Study of the Chain Conformation of the Liquid nParaffins and Molten Polyethylene. *J. Chem. Phys.* **47**, 1316–1360 (1967).
59. Kundu A, Fingerhut BP, Elsaesser T. Hydration structure and dynamics of phosphoric acid and its anions—Ultrafast 2D-IR spectroscopy and ab initio molecular dynamics simulations. *J. Chem. Phys.* **161**, No. 084503 (2024).
60. Li C-Y*, et al.* In situ probing electrified interfacial water structures at atomically flat surfaces. *Nat. Mater.* **18**, 697–701 (2019).
61. Sun C, Xu D, Xue D. In situ FTIR-ATR observation of structural dynamics of $H_2PO_4^-$ in precrystallisation solution. *Mater. Res. Innov.* **18**, 370–375 (2014).
62. Vilčiauskas L, Tuckerman ME, Bester G, Paddison SJ, Kreuer K-D. The mechanism of proton conduction in phosphoric acid. *Nat. Chem.* **4**, 461–466 (2012).
63. Xie J, Liang Z, Lu Y-C. Molecular crowding electrolytes for high-voltage aqueous batteries. *Nat. Mater.* **19**, 1006–1011 (2020).
64. Stephens PJ, Jalkanen KJ, Devlin FJ, Chabalowski CF. Ab initio calculation of vibrational circular dichroism spectra using accurate post-self-consistent-field force fields: trans-2,3-dideuteriooxirane. *J. Phys. Chem.* **97**, 6107–6110 (1993).
65. Hehre WJ, Ditchfield R, Pople JA. Self—Consistent Molecular Orbital Methods. XII. Further Extensions of Gaussian—Type Basis Sets for Use in Molecular Orbital Studies of Organic Molecules. *J. Chem. Phys.* **56**, 2257–2261 (1972).
66. Hariharan PC, Pople JA. The influence of polarization functions on molecular orbital hydrogenation energies. *Theor. Chim. Acta* **28**, 213–222 (1973).
67. Frisch MJ, Pople JA, Binkley JS. Selfconsistent molecular orbital methods 25. Supplementary functions for Gaussian basis sets. *J. Chem. Phys.* **80**, 3265–3269 (1984).
68. Grimme S. Density functional theory with London dispersion corrections. *Wires Comput Mol. SCI.* **1**, 211–228 (2011).
69. Grimme S, Ehrlich S, Goerigk L. Effect of the damping function in dispersion corrected density functional theory. *J. Comput. Chem.* **32**, 1456–1465 (2011).

70. Marenich AV, Cramer CJ, Truhlar DG. Universal Solvation Model Based on Solute Electron Density and on a Continuum Model of the Solvent Defined by the Bulk Dielectric Constant and Atomic Surface Tensions. *J. Phys. Chem. B* **113**, 6378–6396 (2009).
71. Lu T, Chen F. Multiwfn: A multifunctional wavefunction analyzer. *J. Comput. Chem.* **33**, 580–592 (2012).
72. Lu T. A comprehensive electron wavefunction analysis toolbox for chemists, Multiwfn. *J. Chem. Phys.* **161**, 082503 (2024).
73. Lu T, Chen F. Quantitative analysis of molecular surface based on improved Marching Tetrahedra algorithm. *J Mol. Graph. Model.* **38**, 314–323 (2012).
74. Humphrey W, Dalke A, Schulten K. VMD: Visual molecular dynamics. *J. Mol. Graph.* **14**, 33–38 (1996).

Figures

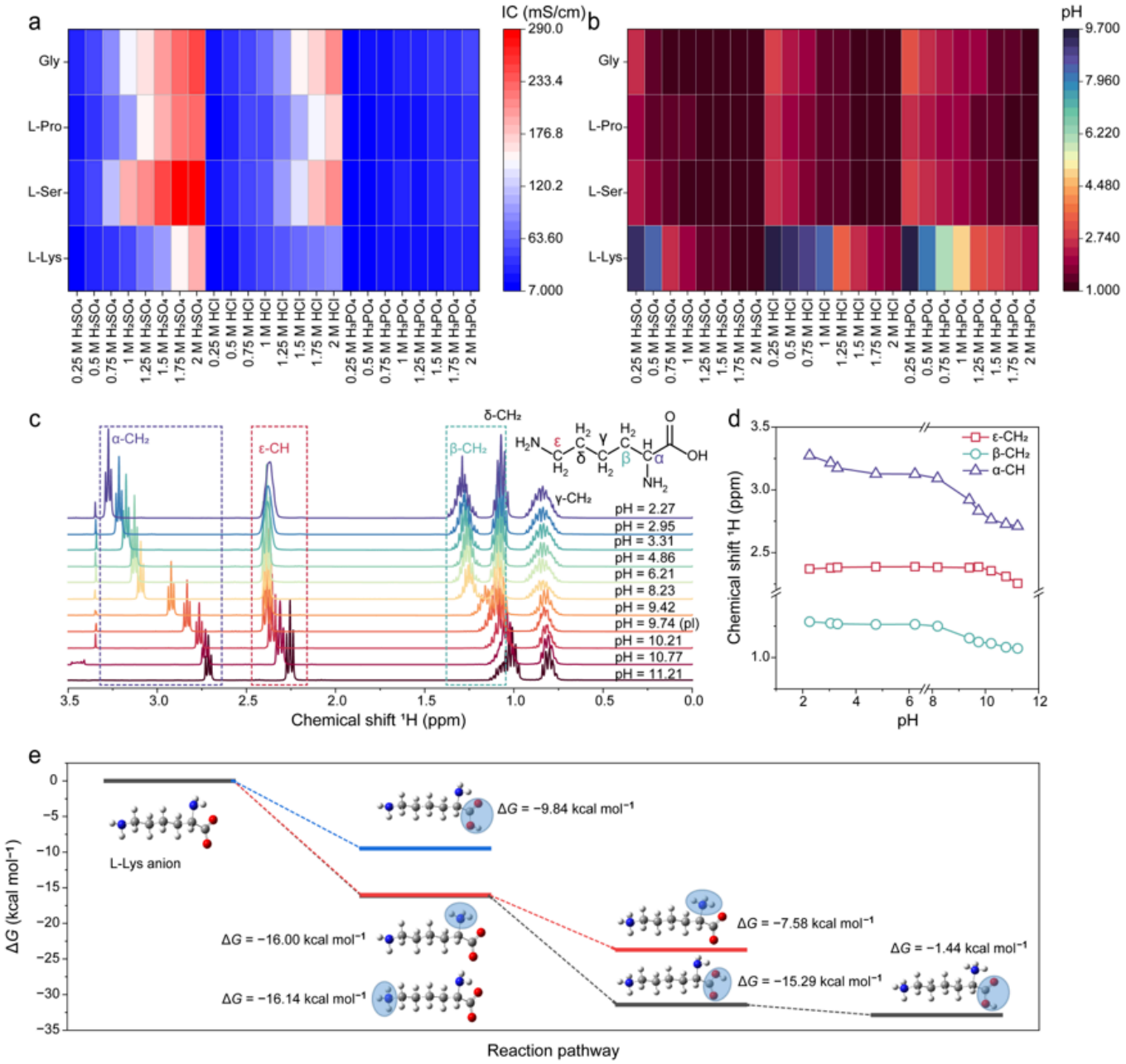


Figure 1

Screening of amino acid salt electrolytes used for near-neutral aqueous proton batteries and the physicochemical and computational properties of L-Lys phosphate electrolytes. Variation of (a) the ionic conductivity and (b) the pH value of the twelve kinds of amino acid salt electrolytes with inorganic acid concentration; (c) ^{1}H NMR spectra of 1 M L-Lys aqueous solutions with different pH values adjusted through H_3PO_4 or KOH and (d) plots of the ^{1}H δ of the ε-CH_2, the β-CH_2, and the α-CH as a function of pH; (e) Gibbs free energy diagram of a L-Lys anion being protonated step by step.

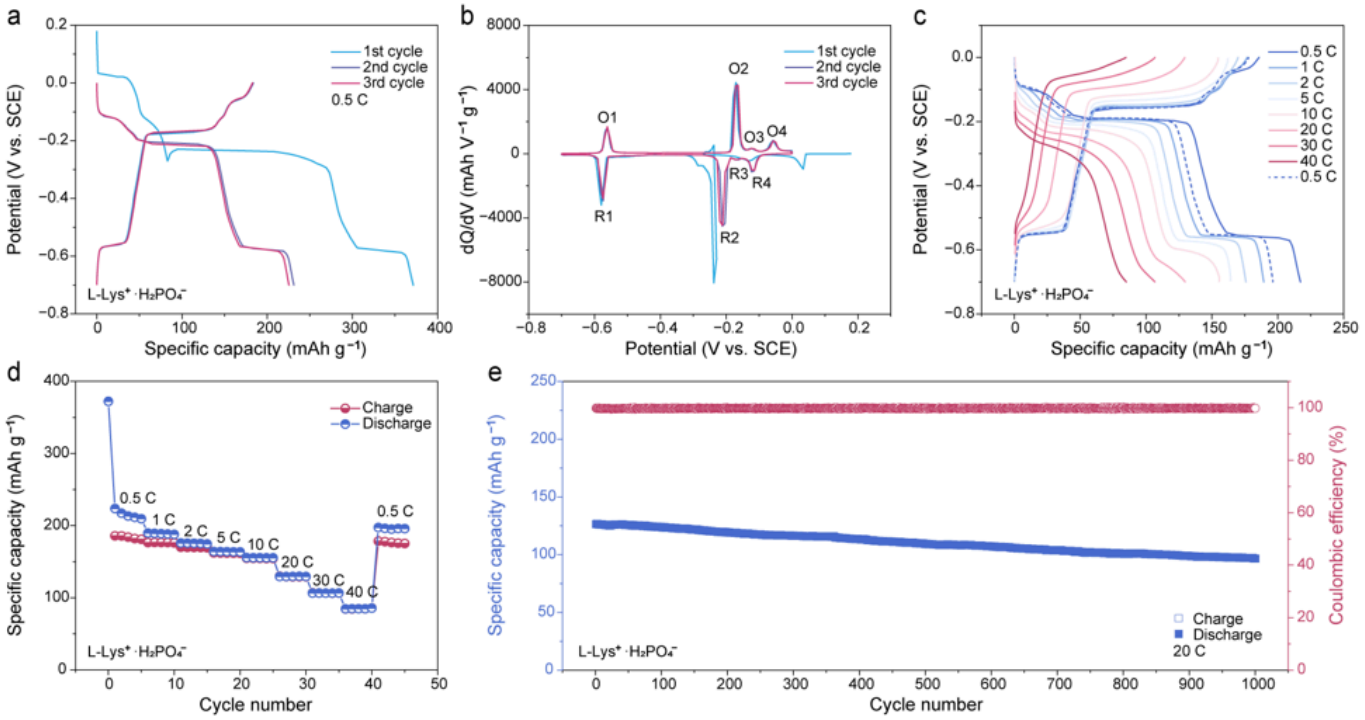


Figure 2

Electrochemical performance of the α-MoO_3 electrode in the L-Lys phosphate electrolyte (1 M L-Lys + 1.25 M H_3PO_4). (a) GCD curves of the first three cycles at 0.5 C (1 C = 372 mA g^{-1}) and (b) the corresponding dQ/dV curves; (c) GCD curves and (d) the corresponding specific capacities at different current densities; (e) Cycling stability measurement at 20 C.

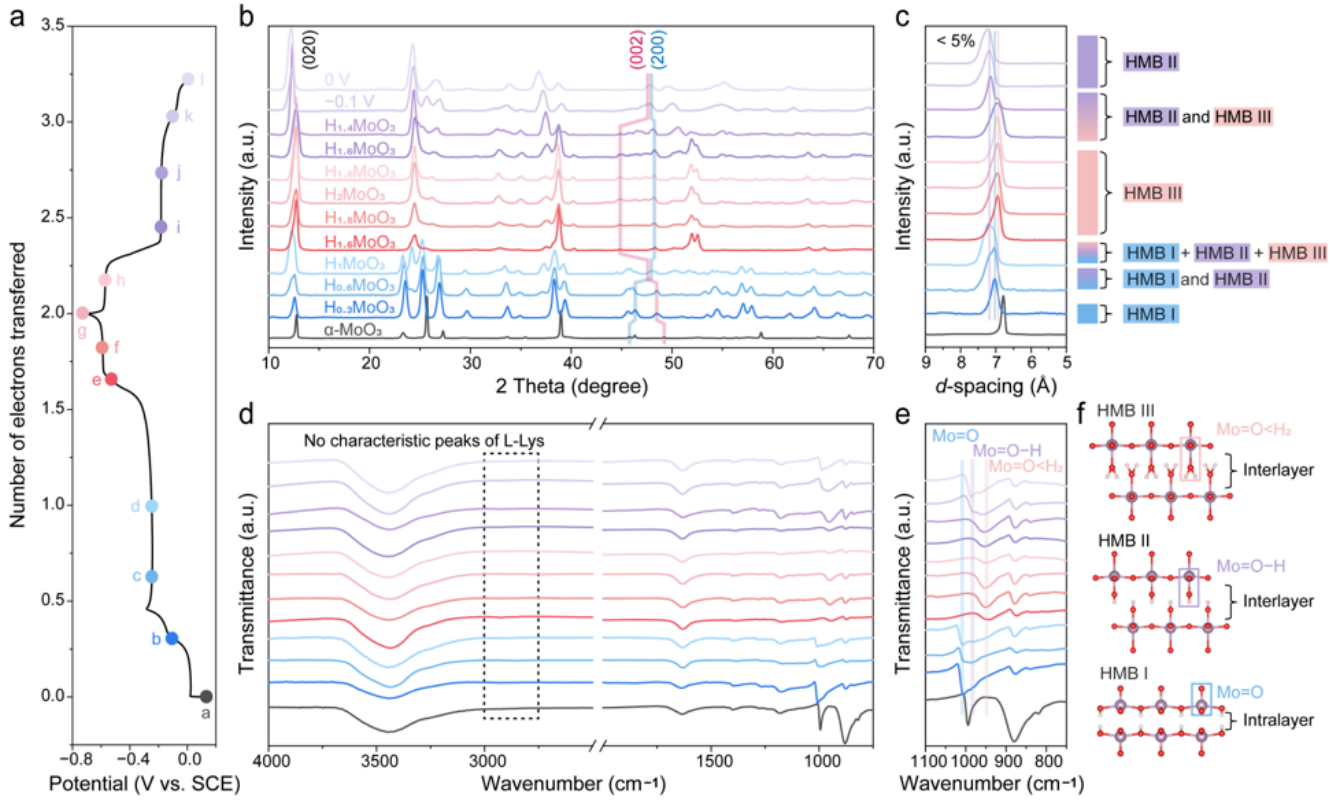


Figure 3

Analysis on the charge storage mechanisms of the α-MoO_3 electrode during the initial cycle in the L-Lys phosphate electrolyte by *ex-situ* XRD and FTIR. (a) Selected states of charge; (b) XRD patterns of the α-MoO_3 electrode at the different states of charge; (c) Magnified XRD patterns in the region that involves the (020) diffraction peak; (d) FTIR spectra of the α-MoO_3 electrode at the different states of charge; (e) Magnified FTIR spectra within a wavenumber range of 1100 to 700 cm^{-1}; (f) Schematic illustration of the occupancy of the protons in the HMB I (bottom), II (middle), and III (top) phases, respectively.

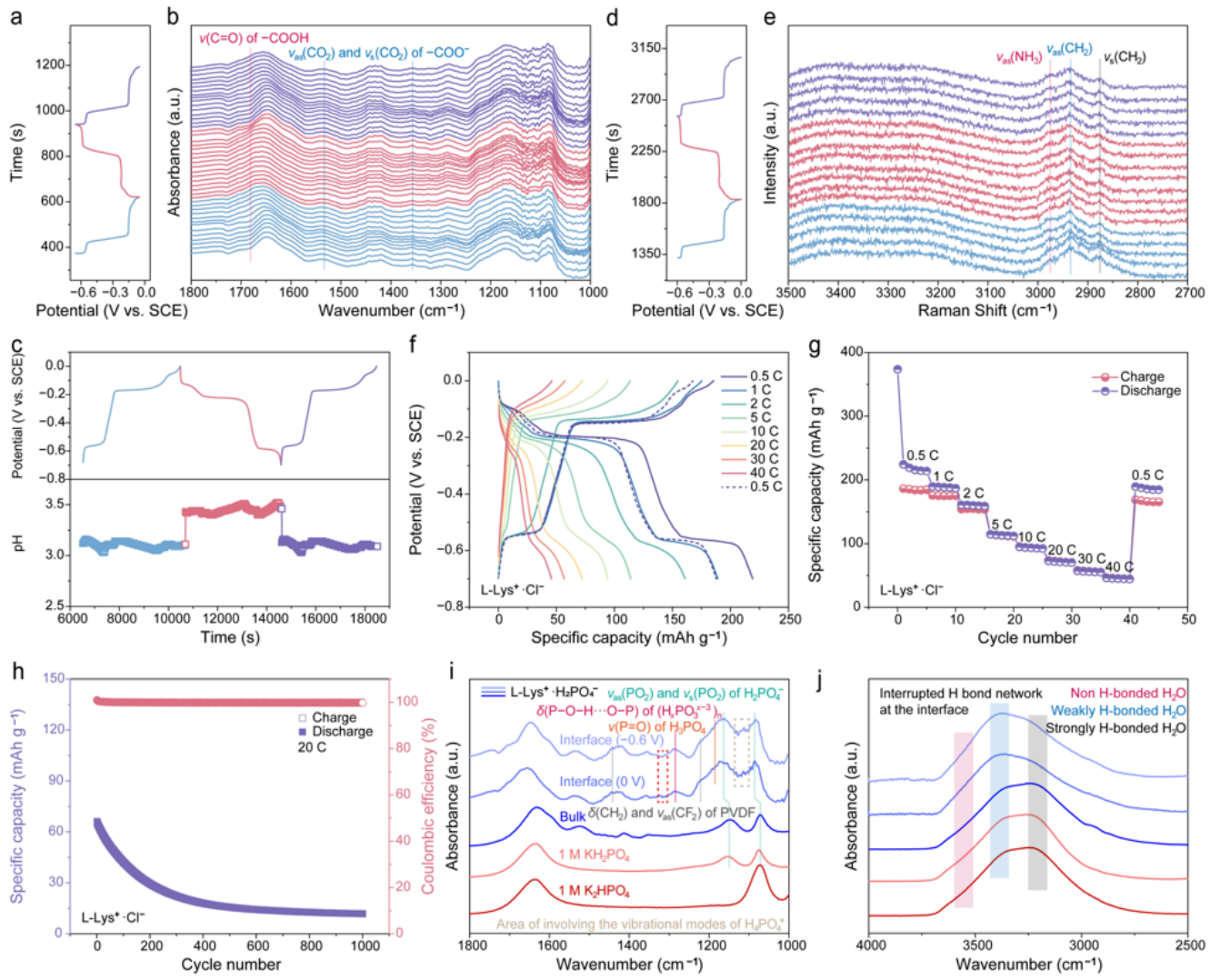


Figure 4

Investigation into the proton transport behavior at the electrochemical interface of the L-Lys phosphate electrolyte in electrochemical events. (a, b) ATR-SEIRAS and (d, e) SERS spectra *in-situ* collected from the electrochemical interface constituted by the α-MoO_3 electrode and the L-Lys phosphate electrolyte; (c) *In-situ* pH monitoring at the above electrochemical interface; (f) GCD curves and (g) the corresponding specific capacities at different current densities as well as (h) the cycling stability measurement at 20 C of the α-MoO_3 electrode in the L-Lys hydrochloride electrolyte (1 M L-Lys + 1.25 M HCl); Comparison of the IRAS spectra of the L-Lys phosphate electrolyte at the electrochemical interface and in the bulk phase, 1 M KH_2PO_4, and 1 M K_2HPO_4 within wavenumber ranges of (i) 1800 to 1000 cm^{-1} and (j) 4000 to 2500 cm^{-1}, respectively.

Supplementary Files

This is a list of supplementary files associated with this preprint. Click to download.

- SupportingInformation.docx
- SupportingInformationanonymized.docx